



HAL
open science

Yearly and seasonal variations of low albedo surfaces on Mars in the OMEGA/MEx dataset: constraints on aerosols properties and dust deposits

Mathieu Vincendon, Y. Langevin, F. Poulet, A. Pommerol, M. Wolff, J.-P. Bibring, B. Gondet, D. Jouglet

► To cite this version:

Mathieu Vincendon, Y. Langevin, F. Poulet, A. Pommerol, M. Wolff, et al.. Yearly and seasonal variations of low albedo surfaces on Mars in the OMEGA/MEx dataset: constraints on aerosols properties and dust deposits. *Icarus*, 2009, 200 (2), pp.395. 10.1016/j.icarus.2008.12.012 . hal-00517246

HAL Id: hal-00517246

<https://hal.science/hal-00517246>

Submitted on 14 Sep 2010

HAL is a multi-disciplinary open access archive for the deposit and dissemination of scientific research documents, whether they are published or not. The documents may come from teaching and research institutions in France or abroad, or from public or private research centers.

L'archive ouverte pluridisciplinaire **HAL**, est destinée au dépôt et à la diffusion de documents scientifiques de niveau recherche, publiés ou non, émanant des établissements d'enseignement et de recherche français ou étrangers, des laboratoires publics ou privés.

Accepted Manuscript

Yearly and seasonal variations of low albedo surfaces on Mars in the OMEGA/MEx dataset: constraints on aerosols properties and dust deposits

Mathieu Vincendon, Y. Langevin, F. Poulet, A. Pommerol, M. Wolff, J.-P. Bibring, B. Gondet, D. Jouglet

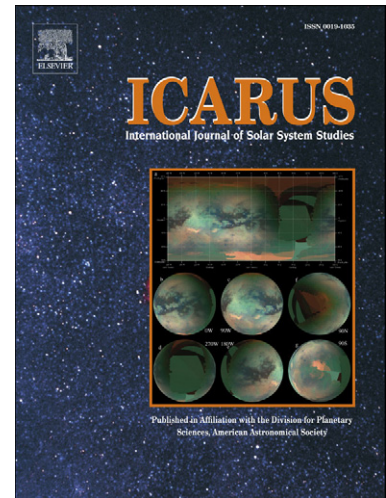
PII: S0019-1035(08)00438-7
DOI: [10.1016/j.icarus.2008.12.012](https://doi.org/10.1016/j.icarus.2008.12.012)
Reference: YICAR 8848

To appear in: *Icarus*

Received date: 18 June 2008
Revised date: 5 December 2008
Accepted date: 11 December 2008

Please cite this article as: M. Vincendon, Y. Langevin, F. Poulet, A. Pommerol, M. Wolff, J.-P. Bibring, B. Gondet, D. Jouglet, Yearly and seasonal variations of low albedo surfaces on Mars in the OMEGA/MEx dataset: constraints on aerosols properties and dust deposits, *Icarus* (2009), doi: [10.1016/j.icarus.2008.12.012](https://doi.org/10.1016/j.icarus.2008.12.012)

This is a PDF file of an unedited manuscript that has been accepted for publication. As a service to our customers we are providing this early version of the manuscript. The manuscript will undergo copyediting, typesetting, and review of the resulting proof before it is published in its final form. Please note that during the production process errors may be discovered which could affect the content, and all legal disclaimers that apply to the journal pertain.



Yearly and seasonal variations of low albedo surfaces on Mars in the OMEGA/MEx dataset: constraints on aerosols properties and dust deposits

Mathieu Vincendon¹, Y. Langevin¹, F. Poulet¹, A. Pommerol², M. Wolff³, J-P. Bibring¹, B. Gondet¹, D. Jouglet¹

¹Institut d'Astrophysique Spatiale, CNRS/Université Paris Sud, Orsay, France.

²Laboratoire de Planétologie de Grenoble, UJF/CNRS, Bât. D de Physique, B.P. 53, 38041 Grenoble Cedex 9, France.

³Space Science Institute, 18970 Cavendish Road, Brookfield, WI 53045, USA.

1

2

3 Number of pages: 37

4 Number of Figures: 15

5 Number of Tables: 2

1 Apparent variations of dark surfaces: the role of aerosols

2 Mathieu Vincendon

3 Institut d'Astrophysique Spatiale

4 Université de Paris Sud

5 Bâtiment 121

6 91405 Orsay

7 France

8 mathieu.vincendon@ias.u-psud.fr

ACCEPTED MANUSCRIPT

1 **Abstract**

2 The time variations of spectral properties of dark Martian surface features are investigated using the OMEGA
3 near-IR dataset. The analyzed period covers two Mars years, spanning from early 2004 to early 2008 (includes
4 the 2007 global dust event). Radiative transfer modeling indicates that the apparent albedo variations of low to
5 mid-latitude dark regions are consistent with those produced by the varying optical depth of atmospheric dust as
6 measured simultaneously from the ground by the Mars Exploration Rovers. We observe only a few significant
7 albedo changes that can be attributed to surface phenomena. They are small-scaled and located at the boundaries
8 between bright and dark regions. We then investigate the variations of the mean particle size of aerosols using
9 the evolution of the observed dark region spectra between 1 μm and 2.5 μm . Overall, we find that the observed
10 changes in the spectral slope are consistent with a mean particle size of aerosols varying with time between 1 μm
11 and 2 μm . Observations with different solar zenith angles make it possible to characterize the aerosol layer at
12 different altitudes, revealing a decrease of the particle size of aerosols as altitude increases.

13

14

15 MARS, ATMOSPHERE

16 MARS, SURFACE

17 MARS, CLIMATE

18 RADIATIVE TRANSFER

19 INFRARED OBSERVATIONS

20

1 **1 Introduction**

2 The atmosphere of Mars constantly contains suspended dust particles that interact in a complex manner with the
3 surface (Sagan et al., 1972). These aerosols are associated with dust deposits on bright regions. Therefore, the
4 settling of aerosols after major storms is expected to increase the albedo of dark regions (Balme et al., 2003;
5 Kinch et al., 2007). The increasing contrast of the main low albedo features in the first few months after the
6 storm season has been attributed to an efficient clean-up process over these dark regions (Sagan et al., 1972;
7 Pleskot and Miner, 1981; Greeley et al., 2005; Rogers et al., 2007). Competitive deposition and clean-up is
8 expected at boundaries between dark and bright regions (Geissler et al., 2008), which results in slow changes of
9 the shape and extent of dark regions (Sagan et al., 1972; Lee, 1986; Christensen, 1988; Geissler 2005; Szwasz et
10 al., 2006). Such long term changes have an impact on the overall radiative balance, and hence, the climate of
11 Mars (Cantor et al., 2007; Fenton et al., 2007).

12

13 Albedo maps provided by IRTM onboard Viking for a period covering a complete Martian year during which a
14 global dust storm occurred have been analyzed by Pleskot and Miner (1981), who concluded that most large-
15 scale variations of surface albedos seen from orbit can be attributed to variations of the atmospheric dust content.
16 Mallama (2007) also observed that apparent albedo variations are strongly influenced by aerosol variations.
17 These variations of the reflectance are strongly dependent on particle size in the near-infrared (Drossart et al.,
18 1991). Clancy *et al.* 2003 defined three regimes with different mean grains size from TES data at low to mid-
19 latitudes (45°S – 45°N) depending on latitude, solar longitude and optical depth. In a companion paper, Wolff
20 and Clancy (2003) showed a distinct increase in the mean particle size associated with the onset of the 2001
21 global dust event. More recently, Wolff et al. (2006) and Soderblom et al. (2008) observed variations of the
22 mean particle size at the MER landing sites, higher mean particle size being observed during periods of higher
23 opacities.

24

25 In this paper, we investigate the variations with time of the apparent surface reflectance over low albedo regions
26 in the low to mid-latitudes using OMEGA/MEx observations. The OMEGA dataset consists of hyperspectral
27 images with a spatial resolution ranging from 300m to 5km, with a wavelength range from 0.3 μm to 5.1 μm .
28 OMEGA has been operating since early 2004, providing more than two Martian years of data, including the
29 2007 high opacity dust storms. Most of the planet has been observed at a low spatial resolution (km scale), with

1 frequent overlaps. These observations confirmed the major role of aerosols in the near-IR spectral range
2 (Drossart et al., 2005, Vincendon et al., 2007). Therefore, one must explicitly consider the effects of aerosols
3 when interpreting observations in this spectral range in terms of surface characteristics.

4
5 In our analysis, we first construct time series of OMEGA observations of different dark regions of Mars at low to
6 mid-latitudes (section 2). Next, we modeled the observed variations of the reflectance with time and/or
7 photometric angles using a multiple-scattering radiative transfer code (section 3). Simultaneous PanCam/MER
8 measurements of the optical depth are considered for comparison. Results are then discussed in terms of surface
9 dust deposit occurrences and aerosols size variations (section 4).

10 **2 Observations**

11 **2.1 The OMEGA dataset**

12 The *Observatoire pour la Minéralogie, l'Eau, les Glaces et l'Activité* (Bibring et al., 2004) has observed almost
13 the entire planet with a resolution of 2 to 5 km, beginning in January 2004. High-resolution observations
14 ($\geq 300\text{m}$), performed during the lowest altitude portions of the Mars Express orbit, cover almost 10% of the
15 surface. The number of overlapping tracks increases at high latitudes with the nearly polar orbit of Mars Express.
16 Most terrains have been observed at least two times, with a set of locations observed as many as ten times. Most
17 observations of mid-latitude dark terrains ($40^\circ\text{S} - 40^\circ\text{N}$) are obtained with the nominal nadir-pointing mode. In
18 this configuration, the phase angle is equal to the solar zenith angle, which varies in a complex manner
19 depending upon the latitude, the season and the local time of the observation. When the 3-axis drift mode is
20 implemented for high altitudes of Mars Express ($>4500\text{km}$), OMEGA performed observations with emergence
21 angles (also known as emission angles) that significantly depart from nadir. Additional non-nadir observations of
22 the Martian surface have also been obtained during limb scans.

23
24 The OMEGA wavelength range ($0.3\mu\text{m} - 5.1\mu\text{m}$) corresponds to the maximum of light scattered by dust
25 aerosols on Mars (e.g. Erard et al., 2001), which also includes several diagnostic features of water ice ($1.5\mu\text{m}$,
26 $2\mu\text{m}$, $3\mu\text{m}$). OMEGA is therefore ideally suited for the study of Martian aerosols.

27
28 The reflectance of dark surfaces at a given wavelength λ is defined by the “reflectance factor” (hereafter noted
29 $\text{RF}(\lambda)$) defined by $I(\lambda)/(\text{Fcos}(i))$; where i is the solar incidence angle, or solar zenith angle, measured from the

1 normal to the reference ellipsoid). $RF(\lambda)$ corresponds to the albedo for a lambertian surface. All observations of
2 a same terrain should have the same RF if: the surface is lambertian, the surface properties do not change with
3 time, and the atmosphere is free of aerosols.

4 **2.2 Constraints for selecting observations**

5 Selected regions of interest correspond to surface albedo at $1 \mu\text{m}$ of 15% or less. The selection of the spectra
6 constituting our time series for a given dark region requires the careful consideration of the following points:

7
8 - We have restricted our analysis to regions for which at least one observation is available at a time when the
9 contribution of aerosols as observed by the Mars Exploration Rovers is low (effective optical depth $-\tau/\cos(i)$ –
10 less than 0.6). This observation will be used to estimate of the actual dependence of the reflectance of the area
11 with wavelength.

12
13 - The contribution of aerosols varies with the incidence angle measured from the normal to the reference
14 ellipsoid, whereas the contribution of the surface is linked with the local incidence angle, which is dependent on
15 local slopes. We therefore need to constrain our analysis to relatively flat regions. This is checked with the
16 MOLA elevation measurements (Smith et al., 1999), which does not preclude local slopes or shadows at smaller
17 scales.

18
19 - High-resolution tracks (width of about 5 – 20 km) can cover homogeneous terrains at slightly different
20 locations (a few kilometers apart). In order to increase the time resolution of our sequences, we have included
21 non-overlapping observations after checking that reflectance properties were similar to the nominal region, as
22 illustrated in Fig. 1.

23
24 - Observations with significant contributions from ice-rich aerosols are not included in the time series. They
25 can be detected from the presence of weak absorption bands at $1.5 \mu\text{m}$ and $2 \mu\text{m}$, and a stronger absorption band
26 at $3 \mu\text{m}$ (Langevin et al., 2007), as shown in Figure 3. Fortunately, water ice aerosols are not detected frequently
27 in OMEGA observations as most dark regions are found south of the aphelion cloud belt (*Figure 2*).

28
29 - The nadir observations take into account photons coming from the surface within the IFOV, and a small
30 fraction of photons coming from nearby areas that are then scattered by aerosols into the IFOV (Langevin et al.,

1 2008). Monte-Carlo simulations using the model of Vincendon et al. (2007a) demonstrates that this contribution
2 becomes negligible at distances of 25 km or more from the IFOV. We have therefore selected regions of interests
3 with variations of the albedo lower than 0.01 over a circle 50 km in diameter.

4 **2.3 Selected time series of observations**

5 The locations of the 14 time series defined from the selection procedure presented in section 2.2 are indicated on
6 Fig. 2.

7 An example of a time series (black stars on the map) showing a wide variety of reflectance spectra is presented
8 in Fig. 3 for the $[0.3 \mu\text{m} - 4 \mu\text{m}]$ wavelength range. In general, we observe significant variation in spectral
9 slopes between $1 \mu\text{m}$ and $2.5 \mu\text{m}$ (from nearly flat spectra to spectral slope of 40%) and albedo levels (from 0.1
10 to 0.3 in the red / $1 \mu\text{m}$ range). Observations with steep blue spectral slopes and strong increase of the reflectance
11 factor correspond to those that include a large contribution of scattering by aerosols (dust storm or high solar
12 zenith angles). In the next section, we present modeling results, which aim to determine whether part or all of the
13 observed spectral variations can be attributed to aerosol effects. We focus on the near IR range ($0.9 \mu\text{m}$ to 2.6
14 μm) which corresponds to one of the three detectors of OMEGA (the C-channel). This spectral range provides
15 typically the strongest constraints on the size of aerosols (Clancy et al., 2003); it can be compared to visible
16 studies as the effect of aerosols varies weakly between 0.7 and $0.9 \mu\text{m}$ (Ockert-Bell et al., 1997; Tomasko et al.,
17 1999) and it is free of thermal contribution. Also of note is the fact that the C-channel is the detector with the
18 lowest radiometric or geometric uncertainties (Bellucci et al., 2006; Jouglet et al., 2008), making comparisons
19 more precise.

20 **3 Modeling assumptions**

21 In this section, we present models of the observed spectra under the assumption that the surface reflectance does
22 not change with time. The results in terms of the derived aerosol parameters will be compared to the ground truth
23 provided by MER/PanCam measurements (Lemmon et al., 2004) and discussed in section 4. We model Martian
24 spectra observed by OMEGA using the Monte-Carlo based approach developed by Vincendon et al. (2007,
25 2008). This type of algorithm simulates the path of photons through a layer containing aerosols, including
26 interactions with the surface. Multiple scattering is handled explicitly, with no simplifying assumptions. The
27 geometry of the model is one-dimensional plane-parallel. The surface reflectance is characterized by a prescribed

1 photometric function and albedo. Three parameters describe the optical behavior of aerosols: the single
2 scattering albedo, the single scattering phase function and the total optical depth. These five parameters are a
3 priori wavelength dependent. Our approach involves the use of look-up tables of apparent reflectance factors,
4 built by simulating the path of a large number of photons (typically 10^6) for each set of input parameters and
5 observing geometries. The removal of gas bands is performed using the “OMEGA volcano-scan approach”
6 described in Langevin et al. (2007). In this method, the observed spectra are divided by a typical atmospheric
7 spectrum scaled to the path length of photons in the atmosphere for each given observation.

8 **3.1 Surface photometric function**

9 Because our observations for a given location were obtained under different illumination conditions, it is useful
10 to investigate the expected variations of the surface contribution with photometric angles. Johnson et al. (2006a,
11 2006b) have extensively studied the photometric properties of different surface textures observed at both MER
12 landing sites. Observed surface behaviors in the visible wavelengths depart from the Lambert case by at most
13 $\pm 10\%$ in the $[25^\circ - 90^\circ]$ range of phase angles, the surface reflectance generally increasing in the anti-solar
14 direction. For the data considered here, the variations of the phase angle are due generally to changes in the solar
15 zenith angle. Given the limited range of the photometric angles in our dataset, it is difficult to generalize the
16 results of Johnson et al. for our modeling efforts. However, recent laboratory measurements provide some
17 guidance. Pommerol and Schmitt (2008) designed a set of laboratory experiments to study the photometric
18 properties of the Martian surface in the near-IR wavelengths, using a spectro-gonio-radiometer (Brissaud et al.,
19 2004). We have extracted from their measurements those corresponding to the geometry of most of our
20 observations: normal emergence with various incidence angles. In addition, we have obtained measurements of
21 two new surface analogues specifically for this study (Fig. 4). The photometric properties of the selected
22 analogues do not vary significantly with wavelength in the $1\mu\text{m} - 2.5\mu\text{m}$ range. Variations of the RF with
23 incidence ($\pm 4\%$ in the $25^\circ - 70^\circ$ range for the surface analogues considered here) are at least one order of
24 magnitude lower than the observed variations in our time series. Therefore, a Lambertian behavior represents a
25 good first approximation for the martian surface as observed with varying solar incidence angle. Additional
26 justification for this assumption may be seen in the fact that the photons reaching a martian surface element
27 sample a wide range of effective incidence angles (Clancy and Lee, 1991). This perturbation from the canonical
28 solar incidence angle is due to aerosol scattering before photons reach the surface. We have characterized this
29 distribution of arrival angles at the surface through our Monte-Carlo code (Fig. 5). In effect, 40% of photons
30 reaching the surface have been scattered outside the original solar direction for a solar incidence angle i of 10°

1 and a moderate optical depth of 0.6. This fraction is larger than 70% at $i=70^\circ$. Consequently, the behavior of the
2 Martian surface as a function of the solar zenith angle is even closer to a Lambert surface than estimated from
3 measurements at well-defined incidence angles.

5 3.2 Assumptions on the optical properties of aerosols

6 We observe variations of the spectral slope of dark regions with time and photometric angles (Fig. 3). If the
7 surface does not change, this requires variations of the aerosol properties. Solar longitudes and solar zenith angle
8 vary simultaneously in our sequences. In Fig. 6, we evaluate the amplitude of the spectral slope variations with
9 solar zenith angle due to expected variations of the phase function of aerosols with wavelength. We computed
10 two wavelength dependent phase functions using the code of Mishchenko and Travis (1998). We considered two
11 potential Martian dust aerosol size distributions: 1 – a bimodal distribution of spherical particles that combine
12 large aerosols generally seen during storms (Toon et al., 1977; Clancy et al., 2003) and a smaller particle size
13 generally seen as the altitude increases (Chassefière et al., 1992; Montmessin et al., 2006; Rannou et al., 2006); 2
14 – a size distribution with a mean particle size of 1.4 μm of randomly oriented oblate cylinders with a 2:1 axial
15 ratio (Wolff et al., 2006). Indices of refraction are taken from Ockert-Bell et al. (1997). Weak variations of the
16 phase function with wavelength are inferred from these models. This results in a ratio of light scattered by
17 aerosols at 1 μm to light scattered at 2.6 μm that ranges between 1.1 and 1.3 (Fig. 6), while this ratio varies
18 between 1 and 4 for our spectra. This suggests that observed variations of the spectral slope may not be
19 predominantly due to variations of the phase function with wavelength. As a result, for simplicity, we will adopt
20 a wavelength independent phase function. Two phase functions retrieved on Mars in the near-IR by other authors
21 will be tested: a Henyey-Greenstein function with an asymmetry parameter of 0.63 (retrieved by Ockert-Bell et
22 al. 1997 between 1 μm and 2.5 μm) and the phase function derived by Tomasko et al. (1999) at 0.965 μm . We
23 have selected a constant single scattering albedo of 0.97 according to Vincendon et al., 2007. This value has
24 been recently confirmed by other authors using different approach or dataset (Wolff et al., 2007; Määttänen et
25 al., submitted to Icarus). The last aerosol parameter to consider is the extinction cross section, being proportional
26 to the optical depth. We treat it as a free, wavelength dependent parameter, as expected from size variations of
27 aerosols (see e.g. Clancy et al., 2003, figure 13).

4 Interpretation of the observed spectra in terms of aerosol properties and surface variations.

For each time series, we estimate the surface albedo spectrum from the observation with the lowest aerosol contribution. These observations are obtained during clear atmospheric conditions ($L_S \sim 30^\circ - 130^\circ$). Even in this case, we performed a small aerosol correction to the data. The low to mid-latitude optical depth is relatively homogeneous in that L_S range (Smith, 2004). We can therefore use the optical depth determined at $0.9 \mu\text{m}$ by MER/PanCam measurements (Lemmon et al., 2004, 2006) at the time of the observation. Optical depths at other wavelengths are derived using the “typical” aerosol wavelength dependent cross section retrieved previously from other locations with OMEGA (the optical depth monotonically decreases between $1 \mu\text{m}$ and $2.65 \mu\text{m}$ by a factor of 1.9; Vincendon et al., 2007b, 2008). Uncertainties resulting from these approximations will be discussed in section 4.1. With the resulting surface spectrum, we constructed the model spectra that provided the best fit of each observation by adjusting the optical depth at $0.9 \mu\text{m}$ as well as the wavelength dependence of the optical depth, where this latter aspect was done through linear combinations of optical depth functions computed with Mie theory for different grain sizes (Clancy et al., 2003, figure 13). We characterize the result of each model fit using two parameters: the optical depth at $0.9 \mu\text{m}$ ($\tau(0.9 \mu\text{m})$), and the “slope factor” S defined by the ratio between the optical depth at $1 \mu\text{m}$ and that at $2.5 \mu\text{m}$.

For illustration purposes, two time series are presented in Fig. 7 and Fig. 8, with the associated retrieved aerosol parameters listed in Table 1 and Table 2. For these two dark areas, the evolution of the spectral properties with time can be well modeled through variations in the optical thickness of aerosols and the assumption of an unchanging surface reflectance.

4.1 Uncertainties

Relative errors on the retrieved parameters are mainly related to the assumptions made when deriving the surface albedo spectrum of each time series. Uncertainties on the optical depths used for the correction (typically ± 0.2) result in uncertainties between $\pm 5\%$ and $\pm 10\%$ for each surface spectrum. Errors due to photometric effects are estimated to be $\pm 2\%$ for most observations (see section 3.1), which do not greatly influence the total uncertainties when combined quadratically. The way these errors propagate to the retrieved parameters τ and S are indicated on Fig. 9, Fig. 13 and Fig. 15. The signal to noise ratio of OMEGA is greater than 100 for most observations (Bibring et al., 2005), which means that corresponding error bars can be neglected.

1
2 Systematic errors result on the one hand from calibration uncertainties of OMEGA data and on the other hand
3 from assumptions about the optical parameters of dust aerosols. OMEGA absolute uncertainties are estimated to
4 be +/- 10%. A shift of +/- 10% on both surface and observed spectra results in optical depth uncertainties of +/-
5 10% for moderate aerosols loading ($\tau(1\mu\text{m}) = 0.5$, $i = 45^\circ$) and of +/- 20% for high aerosols contribution ($\tau(1\mu\text{m})$
6 $= 1$, $i = 75^\circ$). The uncertainty on the single scattering albedo is low (see section 3.2), and the impact of changing
7 the phase function is illustrated in Figure 10.

8 **4.2 Comparison with observations by the Mars Exploration Rovers (MER)**

9 In Fig. 9 and Fig. 10, we compare our retrieved optical depths with nearly-simultaneous measurements by the
10 MERs (Lemmon et al., 2004, 2006 and personal communication). We use the Ockert-Bell et al. (1997) phase
11 function in Fig. 9 and Fig. 10b and the Tomasko et al. (1999) phase function in Fig. 10a. The elevation varies
12 between - 4.5 km and 3 km for the different regions analyzed here. Generally, one considers that optical depth
13 varies with elevation (i.e., surface pressure) when dust is well-mixed in the atmosphere (Zazova et al., 2005).
14 However, it is important to note that the optical depths are often lower at the Spirit landing site compared to
15 those for Opportunity, despite the slightly lower altitude (-1.9km vs. -1.5km). Thus, the altitude does not
16 exclusively control the mean optical depth. Nevertheless, we have scaled all the retrieved optical depths to the
17 elevation of the rover in Fig. 10b. The variations of the modeled optical depth in our data are consistent with
18 those measured by the MERs, regardless of the specific phase function adopted (Fig. 9 and 10a) and of the
19 assumption of elevation variations (Fig. 9 and Fig. 10b). When combined with the evolution of the nominal
20 spectral fits (under the assumption of a single surface reflectance function for each location), the correspondence
21 of the retrieved optical depths of aerosols and the MER measurements strongly suggests that observed spectral
22 variation from observation-to-observation is dominated by aerosol effects.

23 **4.3 Dust deposits at the surface**

24 Assuming the dust deposition rate derived by Kinch et al. (2007) and the optical depths measured by the MERs
25 (Lemmon et al., 2004, 2006 and personal communication), an amount of dust that corresponds to an optical
26 depth of 0.5 (at $0.9\mu\text{m}$) should be deposited at the surface during the 90-sols long decay of the July 2007 global
27 storm. Such dust deposits increase the reflectance factor of the surface from 0.1 to 0.2 (Kinch et al., 2007). The
28 widespread occurrence of such transient bright dust deposits within the analyzed dark regions would therefore
29 have induced a significant overestimation of the optical depth with our method. However, this is not observed

1 (Fig. 9). When taking into account the aerosol contribution and the specific photometric conditions, variations of
2 the surface reflectance by more than a few % are not required in most cases to interpret the observed variations
3 at different epochs (see Fig. 7 and Fig. 8). This implies that the generic situation for dark regions during the
4 2004-2007 period is that either dust does not settle at the surface or dust is rapidly removed once deposited due
5 to surface cleaning mechanisms (Sagan et al., 1972; Pleskot and Miner, 1981; Greeley et al., 2005; Rogers et al.,
6 2007; Cantor et al., 2007). The lack of significant widespread dust deposits after the 2007 planet-encircling dust
7 event contrasts with the large changes in surface albedo reported after the 2001 storm (Smith, 2004; Szwast et
8 al., 2006). Different causes may explain this discrepancy. First, the 2007 dust storm occurred later in the season
9 (between L_S 265° and L_S 325°, compared to L_S 185° – 280°). The efficiency of cleaning processes occurring at
10 dark regions may depend on season. For instance, the dust cover increase at Syrtis lasted until $L_S \sim 320^\circ$ in 2001
11 (Szwast et al., 2006). This L_S corresponds roughly to the end of the 2007 storm, which could explain why no
12 persistent dust cover was detected after the 2007 storm. Secondly, the 2007 storm was shorter compared to that
13 of 2001 (about 60° of L_S versus 95°). Therefore, the amount of raised and settled dust was probably lower.
14 Finally, we must notice that previous study of apparent albedo change do not always account for slight change in
15 aerosols contribution. During clear atmospheric conditions ($\tau_{\text{vis}} \sim 0.4$), a 0.1 change in optical depth from one
16 year to another is enough to simultaneously increase the reflectance at 1 μm of dark regions by 0.01 while
17 decreasing that of the brightest regions by a few 0.001. Such a change mimics a depletion of dust from bright
18 regions and a deposition of dust above dark regions. T-IR optical depths are frequently used to assess similar
19 atmospheric conditions and avoid this kind of mistakes (Szwast et al., 2006). However, a change of the visible
20 optical depth can be undetectable in the thermal infrared if it is associated with a change of the mean particle
21 size. As we will see in the next section, such particle size changes are observed after dust storm (Fig. 15).

22
23 We have searched for localized variations of surface reflectance in OMEGA observations by looking at albedo
24 boundaries of dark regions that are known to undergo surface albedo changes (Geissler, 2005; Szwast et al.,
25 2006) or to be covered by a dust coating (Rogers et al., 2007). Specific areas of interest were selected on the
26 basis of the availability of OMEGA observations after the global dust storms of 2007. OMEGA observations of
27 the Nilosyrtis region obtained in 2004 and 2008 with similar aerosols and lighting conditions are compared on
28 Figure 11. Some areas show constant spectral properties, while some regions brighten (Fig. 12). The observed
29 brightening would imply an optical depth of 1.5 ± 0.15 with our method, while the optical depth is between 0.4
30 and 0.8 at that time. These increases in reflectance are not due simply to serendipitous occurrence of a local dust

1 storms in the field-of-view during the observation, because no changes are observed in the depth of $2 \mu\text{m CO}_2$
2 gas band (which is strongly correlated to the path length of photons in the atmosphere; Bibring et al., 1990).
3 These differences occur on surfaces that manifest a strong negative spectral slope, which can be reproduced in
4 laboratory experiments by a coating of dust (see e.g. Fischer and Pieters, 1993). The presence of such localized
5 dust deposits is consistent with the observations and the analyzes of Sagan et al., (1972) which concluded that
6 dust settles on the surface in specific areas linked with topographic features.

7 **4.4 Variations in the size of aerosols**

8 The decrease in the cross section of aerosols with wavelength becomes steeper as the particle size decreases
9 (Clancy et al., 2003). A relationship between the slope factor S and the mean particle size is derived by
10 computing the scattering properties of aerosols with different effective radius r_{eff} using the T-matrix code of
11 Mishchenko and Travis (1998). We select the scattering properties of randomly oriented oblate cylinders (2:1
12 axial ratio) and a size distribution width $v_{\text{eff}}=0.3$, similarly to Wolff et al. (2006). The refractive indices are taken
13 from Ockert-Bell et al. (1997). We use the factor $\omega Q_{\text{ext}}P(\theta)$ (the product of the single scattering albedo, the
14 extinction cross section and the phase function at an angle θ) instead of the extinction cross section so as to
15 account for the variations of the phase function with wavelength (Fig. 6). $\omega Q_{\text{ext}}P(\theta)$ is proportional to the
16 number of photons scattered once toward the zenith direction for an initial solar incidence angle $\pi - \theta$. This
17 parameter is equivalent to the slope factor S when single scattering dominate.

18
19 The variations of the aerosol size with solar zenith angle are indicated on Fig. 13. Using the slope factor as an
20 indicator of particle size, the effective size retrieved from observations obtained at low to moderate solar zenith
21 angles varies with time in the $1 \mu\text{m}$ to $2 \mu\text{m}$ range. This result is consistent with that obtained by previous authors.
22 Clancy et al. (2003) observed three different mean particle sizes on Mars with TES data: $1 \mu\text{m}$, $1.5 \mu\text{m}$ and 1.8 -
23 $2.5 \mu\text{m}$. Wolff and Clancy (2003) observed variations of r_{eff} with time and space around $1.6 \mu\text{m}$. Wolff et al.
24 (2006) and Soderblom et al. (2008) observed an effective radius of aerosols that range between $1.2 \mu\text{m}$ and 1.8
25 μm at the MER landing sites. The effective particle size appears to decrease to values lower than $1 \mu\text{m}$ as the
26 incidence angle goes past 60° (Fig. 13). In fact, the slope factor derived from observations at extreme solar
27 incidence (80°) implies quite small particle sizes (a few tenths of μm). We have simulated the altitude at which
28 the first interaction with aerosols occurs as a function of the solar incidence angle with our Monte-Carlo model
29 of radiative transfer (Fig. 14). For a typical optical depth range of $0.5 - 1$ (at $0.9 \mu\text{m}$) and a scale height of

1 11.5km that correspond to well-mixed conditions (Lemmon et al., 2004; Zazova et al., 2005), the mode of the
2 altitude distribution increases from 0 (ground) at low to moderate solar incidence angle to 15-20 km for a solar
3 incidence of 80°. Therefore, it may be reasonable to interpret the decrease of the mean particle size with solar
4 incidence angle as a sensitivity of the OMEGA observations to a decreasing particle size with altitude. Several
5 authors have already pointed out such a decrease of the particle size with altitude using ISM/Phobos and
6 SPICAM/Mars Express data. Chassefière et al. (1992) retrieve a vertical gradient of $0.05 \mu\text{m km}^{-1}$ below 25 km
7 for the effective radius of dust particles. Korablev et al. (1993) found that the effective radius decreases from 1.6
8 μm near 15 km to 0.8 μm at 25 km. Montmessin et al. (2006) observe effective radius lower than 0.1 μm above
9 60 km and size larger than 0.3 μm below 50 km, and Rannou et al. (2006) observe dust particles that range
10 between 0.01 and 0.1 μm above 20 km. This decrease in particle size with altitude is generally explained through
11 gravitational settling (e.g., Montmessin et al., 2002). The mean altitude of interaction at high solar zenith angle
12 depends on the optical depth (Fig. 14): when the optical depth is very low (<0.2), most photons interact near the
13 surface even at $i=80^\circ$. This is consistent with the interpretation of large particles at high solar zenith angle and
14 low optical depth (“purple” point at $i=80^\circ$ in Fig. 13, which corresponds to an optical depth of 0.19 at $L_S 54^\circ$).

15

16 Several authors have retrieved higher mean particle sizes during high opacity periods (Clancy et al., 2003; Wolff
17 and Clancy, 2003; Wolff et al., 2006; Soderblom et al., 2008). Such behavior is predicted by numerical
18 simulations (Murphy et al., 1993; Kahre et al., 2008) as larger particles lifted during storms settle faster than
19 smaller particles. In Fig. 15, we have plotted the variation of the particle size as a function of the optical depth
20 for the period covering the maximum and the decay of the global dust storm of 2007 ($L_S 265^\circ - L_S 30^\circ$). Indeed,
21 we observe a decrease of the particle size from 1.5 μm to 1.1 μm as the optical depth decreases after the dust
22 storm, similarly to Wolff and Clancy (2003).

23 5 Conclusions

24 We show that the observed variations of the apparent reflectance of dark surfaces in the OMEGA dataset from
25 2004 to 2007 can be reproduced by variations in the relative contribution of aerosols (due to different lighting
26 conditions and column optical depths). The temporal variations of the optical depths derived from the
27 observations of low to mid-latitudes dark regions ($40^\circ\text{S} - 40^\circ\text{N}$) are consistent with those determined at both
28 MER sites. When combined with the similar evolutions at the two MER sites at longitudes 180° apart, our

1 observations would seem to support the idea that the diffuse component of dust optical depth is relatively
2 homogeneous over low to mid-latitudes and nearly independent of the longitude for a given epoch.

3
4 Widespread transient dust deposits are not observed over dark areas in the near-IR after the major planet
5 encircling dust event of 2007. The decrease of the apparent reflectance of dark surfaces during the decay of dust
6 storms is consistent with that expected from the decrease of the contribution of aerosols. This implies that either
7 dust is not significantly deposited on most dark terrains or dust is rapidly removed by cleaning mechanisms.
8 Localized surface deposits after the 2007 dust storms are observed at the boundaries between bright and dark
9 regions.

10
11 The observed spectral characteristics of aerosols vary with time and photometric angles. Within the framework
12 of our aerosol model, these variations are consistent with changes of the particle size of the aerosols. An
13 effective radius between 1 μm and 2 μm is retrieved from OMEGA nadir observations at low to moderate solar
14 incidence angles. This range corresponds to the variations with time of the mean particle size of the whole
15 aerosols layer. The mean particle size of aerosols decreases during the decrease of the optical depth following
16 the 2007 global dust storm. The apparent particle size seems to decrease significantly ($< 1\mu\text{m}$) for high solar
17 incidence angles. Monte-Carlo radiative transfer simulations suggest that these variations are due to a decrease
18 of the mean particle size with altitude in the bottom 30-40 kilometers of the atmosphere.

19
20 These results have implications for the retrieval of actual surface reflectance properties in the VIS-NIR spectral
21 range by removing the contribution of aerosol scattering (Vincendon et al., 2007a, 2008; McGuire et al., 2008).
22 The optical depths derived by PanCam on both Mars Exploration Rovers provide a useful first estimate of the
23 optical depth for low to mid-latitudes regions, and can be used to evaluate the aerosol contributions for
24 simultaneous observations of Mars in the near IR (OMEGA, CRISM) (Poulet et al., 2008). The implied
25 variations of the particle size with time and altitude could significantly modify the spectral impact of aerosols on
26 retrieved surface properties. Due to the non-repeatability of the Martian dust “cycle”, a simultaneous
27 measurement of the aerosols properties is clearly of interest. For CRISM on MRO, this is available as an
28 Emission Phase Function that is acquired for each targeted observation (Murchie et al., 2007).

1 **Acknowledgment**

2 The authors deeply thank M. T. Lemmon for making his optical depth retrievals available for our study. We
3 would also like to thank Lori Fenton and an anonymous reviewer for useful comments and suggestions.

4 **References**

5 Balme, M. R., P. L. Whelley, and R. Greeley, Mars: Dust devil track survey in Argyre Planitia and Hellas Basin,
6 2003. *J. Geophys. Res.*, 108(E8), 5086, doi:10.1029/2003JE002096.

7

8 Bellucci, G., F. Altieri, J.-P. Bibring, G. Bonello, Y. Langevin, B. Gondet, F. Poulet (2006), OMEGA/Mars
9 Express: Visual channel performances and data reduction techniques. *Planetary and Space Science*, 54, 7, 675-
10 684.

11

12 Bibring, J.-P., and 16 colleagues, ISM observations of Mars and PHOBOS - First results, 1990. Lunar and
13 Planetary Science Conference, 20th, Houston, TX, Mar. 13-17, 1989.

14

15 Bibring, J.-P., and 13 colleagues, Perennial water ice identified in the south polar cap of Mars, 2003. *Nature*,
16 428, 6983, 627-630.

17

18 Bibring, J.-P., and 10 colleagues, Mars Surface Diversity as Revealed by the OMEGA/Mars Express
19 Observations, *Science* 307, 1576 (2005)

20

21 Brissaud O., B. Schmitt, N. Bonnefoy, S. Doute, P. Rabou, W. Grundy, M. Fily (2004), Spectrogonio radiometer
22 for the study of the bidirectional reflectance and polarization functions of planetary surfaces. 1. Design and tests
23 *Appl. opt.*, vol. 43, n°9, pp. 1926-1937.

24

25 Cantor, B. A. (2007), MOC observations of the 2001 Mars planet-encircling dust storm. *Icarus*, 186, 60-96.
26 doi:10.1016/j.icarus.2006.08.019.

27

- 1 Chassefière, E., J. E. Blamont, V. A. Krasnopolsky, O. I. Korablev, S. K. Atreya, R. A. West, Vertical structure
2 and size distributions of Martian aerosols from solar occultation measurements, 1992. *Icarus*, 97, 1, 46-69.
3 doi:10.1016/0019-1035(92)90056-D.
4
- 5 Christensen, P. R., Global albedo variations on Mars - Implications for active aeolian transport, deposition, and
6 erosion, 1988. *J. Geophys. Res.*, 93, 7611-7624.
7
- 8 Clancy, R. T., S. W. Lee (1991), A new look at dust and clouds in the Mars atmosphere: analysis of emission-
9 phase-function sequences from global Viking IRTM observations. *Icarus*, 93, 135-158, doi:10.1016/0019-
10 1035(91)90169-T.
11
- 12 Clancy, R. T., Wolff, M. J., Christensen, P. R., Mars aerosol studies with the MGS TES emission phase function
13 observations: Optical depths, particle sizes, and ice cloud types versus latitude and solar longitude, 2003. *J.*
14 *Geophys. Res.*, 108, E9, 5098.
15
- 16 Drossart, P., J. Rosenqvist, S. Erard, Y. Langevin, J.-P. Bibring, and M. Combes (1991), Martian aerosol
17 properties from the Phobos/ISM experiment, *Annales Geophysicae*, 9, 754-760.
18
- 19 Drossart, P., et al. (2005), Atmospheric studies with OMEGA/Mars Express. Paper presented at the LPSC
20 XXXVI, LPI, Houston, TX. Abstract n°1737.
21
- 22 Fenton, L. K., Geissler, P. E., Haberle, R. M., Global warming and climate forcing by recent albedo changes on
23 Mars, 2007. *Nature*, 446, 7136, 646-649, doi:10.1038/nature05718.
24
- 25 Fischer E. M. and Carle M. Pieters, The Continuum Slope of Mars: Bidirectional Reflectance Investigations and
26 Applications to Olympus Mons, 1993. *Icarus*, 102(2), 185-202.
27
- 28 Geissler, P. E., Three decades of Martian surface changes, 2005. *J. Geophys. Res.*, 110, E02001,
29 doi:10.1029/2004JE002345
30

- 1 Geissler, P. E., Tornabene, L. L., Verba, C., Bridges, N. T., Hirise Team (2008). HiRISE Observations of
2 Martian Albedo Boundaries. Paper presented at the LPSC XXXIX, LPI, Houston, TX. Contribution No. 1391.,
3 p.2352.
4
- 5 Greeley, R., et al. (2005), Martian variable features: New insight from the Mars Express Orbiter and the Mars
6 Exploration Rover Spirit, *J. Geophys. Res.*, 110, E06002, doi:10.1029/2005JE002403.
7
- 8 Johnson, J. R., and 13 colleagues, 2006a. Spectrophotometric properties of materials observed by Pancam on the
9 Mars Exploration Rovers: 1. Spirit, *J. Geophys. Res.*, 111, E02S14, doi:10.1029/2005JE002494.
10
- 11 Johnson, J. R., and 13 colleagues, 2006b. Spectrophotometric properties of materials observed by Pancam on the
12 Mars Exploration Rovers: 2. Opportunity, *J. Geophys. Res.*, 111, E12S16, doi:10.1029/2006JE002762.
13
- 14 Jouglet D., Poulet F., Langevin Y., Bibring J.P., Gondet B., Vincendon M., Berthé M. (2008), OMEGA Long
15 Wavelength channel : data reduction during non-nominal stages, submitted to *Planetary and Space Science*.
16
- 17 Kahre, M. A.; Hollingsworth, J. L.; Haberle, R. M.; Murphy, J. R. (2008), Investigations of the variability of
18 dust particle sizes in the martian atmosphere using the NASA Ames General Circulation Model. *Icarus*, 195, 2,
19 576-597. doi: 10.1016/j.icarus.2008.01.023.
20
- 21 Kinch, K. M., J. Sohl-Dickstein, J. F. Bell III, J. R. Johnson, W. Goetz, and G. A. Landis, 2007. Dust deposition
22 on the Mars Exploration Rover Panoramic Camera (Pancam) calibration targets, *J. Geophys. Res.*, 112, E06S03,
23 doi:10.1029/2006JE002807.
24
- 25 Korablev, O. I., V. A. Krasnopolsky, A. V. Rodin and E. Chassefière, Vertical Structure of Martian Dust
26 Measured by Solar Infrared Occultations from the *Phobos* Spacecraft, *Icarus*, 102(1), 76-87 (1993).
27
- 28 Langevin, Y., J.-P. Bibring, F. Montmessin, F. Forget, M. Vincendon, S. Doute', F. Poulet, and B. Gondet
29 (2007), Observations of the south seasonal cap of Mars during recession in 2004–2006 by the OMEGA

- 1 visible/near-infrared imaging spectrometer on board Mars Express, *J. Geophys. Res.*, 112, E08S12,
2 doi:10.1029/2006JE002841.
3
- 4 Langevin Y., M. Vincendon, F. Poulet, J-P. Bibring, B. Gondet, S. Douté, and T. Encrenaz (2008), Water Ice at
5 High Northern Latitudes: Aerosols, Frosts and Ice Outcrops. Paper presented at the 39th Lunar and Planetary
6 Science conference, Houston, TX.
7
- 8 Lee, S. W., IRTM Thermal and Albedo Observations of Syrtis Major, 1986. Paper presented at the 17th Lunar
9 and Planetary Science conference, Houston, TX.
10
- 11 Lemmon, M. T., et al., Atmospheric imaging results from the Mars Exploration Rovers: Spirit and Opportunity,
12 2004. *Science*, 306, 1753–1756, doi:10.1126/science.1104474.
13
- 14 Lemmon, M. T., et al. (2004), Atmospheric imaging results from the Mars Exploration Rovers: Spirit and
15 Opportunity. *Science*, 306, 1753-1756, doi:10.1126/science.1104474.
16
- 17 Lemmon, M. T., and the Athena Science Team (2006), Mars Exploration Rover atmospheric imaging: dust
18 storms, dust devils, dust everywhere. Paper presented at *LPSC XXXVII*, LPI, Houston, TX.
19
- 20 Määttänen, A., T. Fouchet, O. Forni, R. Melchiorri, F. Forget, H. Savijarvi, J.-P. Bibring, Y. Langevin, B.
21 Gondet, V. Formisano, M. Giuranna, A study of the properties of a local dust storm with Mars Express OMEGA
22 and PFS data, submitted to *Icarus*.
23
- 24 Mallama, Anthony, The magnitude and albedo of Mars, 2007. *Icarus*, 192, 2, 404-416.
25 doi :10.1016/j.icarus.2007.07.011.
26
- 27 Markiewicz, W. J., R. M. Sablotny, H. U. Keller, N. Thomas, D. Titov, and P. H. Smith (1999), Optical
28 properties of the Martian aerosols as derived from Imager for Mars Pathfinder midday sky brightness data. *J.*
29 *Geophys. Res.*, 104, E4, 9009-9018, doi:10.1029/1998JE900033.
30

- 1 Mishchenko, M. I. and L. D. Travis, Capabilities and limitations of a current FORTRAN implementation of the
2 T-matrix method for randomly oriented, rotationally symmetric scatterers. *J. Quant. Spectrosc. Radiat. Transfer*,
3 vol. 60, 309-324 (1998).
4
- 5 McGuire P. C., et al. (2008), MRO/CRISM Retrieval of Surface Lambert Albedos for Multispectral Mapping of
6 Mars with DISORT-based Radiative Transfer Modeling: Phase 1 – Using Historical Climatology for
7 Temperatures, Aerosol Optical Depths, and Atmospheric Pressures. *Transactions on Geoscience and Remote*
8 *Sensing*, submitted.
9
- 10 Montmessin, F., Rannou, P., Cabane, M. (2002), New insights into Martian dust distribution and water-ice cloud
11 microphysics. *J. Geophys. Res.*, 107, E6, 4-1.
12
- 13 Montmessin, F., E. Quemerais, J. L. Bertaux, O. Korablev, P. Rannou, and S. Lebonnois (2006), Stellar
14 occultations at UV wavelengths by the SPICAM instrument: Retrieval and analysis of Martian haze profiles, *J.*
15 *Geophys. Res.*, 111, E09S09, doi:10.1029/2005JE002662.
16
- 17 Murchie, S., et al. (2007), Compact Reconnaissance Imaging Spectrometer for Mars (CRISM) on Mars
18 Reconnaissance Orbiter (MRO), *J. Geophys. Res.*, 112, E05S03, doi:10.1029/2006JE002682.
19
- 20 Murphy, J. R., R. H. Haberle, O. B. Toon, J. B. Pollack (1993), Martian Global Dust Storms: Zonally Symmetric
21 Numerical Simulations Including Size-Dependent Particle Transport, *J. Geophys. Res.*, 98, E2, 3197-3220.
22
- 23 Ockert-Bell, M.E., Bell III, J.F. , Pollack, J. B. , McKay, C. P. , Forget, F., 1997. Absorption and scattering
24 properties of the Martian dust in the solar wavelengths. *J. Geophys. Res.*, 102, E4, 9039-9050.
25
- 26 Palluconi, F.D., Kieffer, H.H, 1981. Thermal inertia mapping of Mars from 60°S to 60°N. *Icarus* 45, 415–426.
27
- 28 Pleskot, L. K.; Miner, E. D., Time variability of Martian bolometric albedo, 1981. *Icarus*, 45, 179-201,
29 doi:10.1016/0019-1035(81)90013-0
30

- 1 Pommerol, A., B. Schmitt (2008), *J. Geophys. Res.*, submitted.
- 2
- 3 Poulet F., J.-P. Bibring, Y. Langevin, J. F. Mustard, N. Mangold, M. Vincendon, B. Gondet, P. Pinet, J.-M.
- 4 Bardintzeff, B. Platevoet (2008), Quantitative compositional analysis of Martian mafic regions using
- 5 MEx/OMEGA reflectance data: 1. Methodology, uncertainties and examples of application, *Icarus*, submitted.
- 6
- 7 Rannou, P., S. Perrier, J.-L. Bertaux, F. Montmessin, O. Korablev, and A. Reberac (2006), Dust and cloud
- 8 detection at the Mars limb with UV scattered sunlight with SPICAM, *J. Geophys. Res.*, 111, E09S10,
- 9 doi:10.1029/2006JE002693.
- 10
- 11 Rogers, A. D., J. L. Bandfield, and P. R. Christensen (2007), Global spectral classification of Martian low-
- 12 albedo regions with Mars Global Surveyor Thermal Emission Spectrometer (MGS-TES) data, *J. Geophys. Res.*,
- 13 112, E02004, doi:10.1029/2006JE002726.
- 14
- 15 Sagan, C, J. Veverka, P. Fox, R. Dubisch, J. Lederberg, E. Levinthal, L. Quam, R. Tucker, J. B. Pollack, B. A.
- 16 Smith, Variable Features on Mars : Preliminary Mariner 9 Television Results (1972), *Icarus* 17, 346-372.
- 17
- 18 Smith, D. E., et al., The Global Topography of Mars and Implications for Surface Evolution, 1999. *Science*, 284,
- 19 5419, 1495-1503, doi: 10.1126/science.284.5419.1495
- 20
- 21 Smith, M.D., 2004. Interannual variability in TES atmospheric observations of Mars during 1999–2003. *Icarus*
- 22 167 (1), 148–165.
- 23
- 24 Soderblom, J. M., M. J. Wolff, J. F. Bell III (2008), Temporal variations in the size distribution of Martian
- 25 atmospheric dust from Mars Exploration Rover NavCam observations. Paper presented at the LPSC XXXIX,
- 26 LPI, Houston, TX. Abstract n° 1884.
- 27
- 28 Szwast, M. A., Richardson, M. I., Vasavada, A. R., Surface dust redistribution on Mars as observed by the Mars
- 29 Global Surveyor and Viking orbiters, 2006. *J. Geophys. Res.*, 111, E11008, doi:10.1029/2005JE002485
- 30

- 1 Tomasko, M. G., Doose, L. R., Lemmon, M., Smith, P. H., Wegryn E., 1999. Properties of dust in the Martian
2 atmosphere from the Imager on Mars Pathfinder. *J. Geophys. Res.*, 104, E4, 8987-9008
3
- 4 Toon, O. B.; Pollack, J. B.; Sagan, C., Physical properties of the particles composing the Martian dust storm of
5 1971-1972, *Icarus*, 30, 663-696. (1977).
6
- 7 Vincendon, M., Langevin, Y., Poulet, F., Bibring, J.-P., Gondet, B., 2007a. Recovery of surface reflectance
8 spectra and evaluation of the optical depth of aerosols in the near-IR using a Monte-Carlo approach: Application
9 to the OMEGA observations of high latitude regions of Mars. *J. Geophys. Res.*, 112, E08S13.
10
- 11 Vincendon, M., Langevin, Y., Poulet, F., Bibring, J.-P., Gondet, B., Retrieval of surface Lambert albedos and
12 aerosols optical depths using OMEGA near-IR EPF observations of Mars, 2007b. Paper presented at the LPSC
13 XXXVIII, LPI, Houston, TX.
14
- 15 Vincendon, M., Langevin, Y., Poulet, F., Bibring, J.-P., Gondet, B., Jouglet, D., Dust aerosols above the south
16 polar cap of Mars as seen by OMEGA, 2008. *Icarus*, 196, 488-505, doi:10.1016/j.icarus.2007.11.034.
17
- 18 Wolff, M. J., Clancy, R. T. (2003), Constraints on the size of Martian aerosols from Thermal Emission
19 Spectrometer observations. *J. Geophys. Res.*, 108, E9, 1-1, 5097.
20
- 21 Wolff, M. J., and 12 colleagues, Constraints on dust aerosols from the Mars Exploration Rovers using MGS
22 overflights and Mini-TES, 2006. *J. Geophys. Res.*, 111, E12S17.
23
- 24 Wolff, M.; Clancy, R. T.; Smith, M. D.; Arvidson, R.; Cantor, B.; Kahre, M.; Morris, R.; Seelos,
25 F.Clancy, R. T.; Arvidson, R.; Smith, M. D.; Murchie, S. L.; McGuire, P. C. (2007), Investigating the
26 Wavelength Dependence of the Single-Scattering Albedo of Martian Dust Aerosols with CRISM and MARCI
27 Observations of the Very Dusty Atmosphere in 2007. *American Geophysical Union*, Fall Meeting 2007, abstract
28 #P31D-03.
29

- 1 Zazova, L., and 20 colleagues, Water clouds and dust aerosols observations with PFS MEX at Mars, 2005.
2 *Planet. Space Sci.*, 53(10), 1065-1077.

3 **Tables**

- 4 Table 1: Season, photometric angles and results of the model for observations of Figure 7. The optical depth
5 $\tau(0.9\mu\text{m})$ and the Slope factor S are assumptions for the observation with the lowest optical thickness (black in
6 Figure 7).

Color	Solar Longitude	Mars Year	Incidence	Emergence	Phase	$\tau(0.9\mu\text{m})$	S ("Slope factor")	RMS (%)
Black	39°	27	38°	2°	36°	0.35	1.8	-
dark blue	188°	27	42°	43°	38°	0.69	2.1	0.02
sky blue	254°	27	80°	4°	83°	1.08	3.3	0.06
Green	329°	27	30°	5°	32°	0.99	1.4	0.03
Red	282°	28	40°	1°	40°	2.9	1.6	0.07

7

8

- 9 Table 2 : Season, photometric angles and results of the model for observations of Figure 8. The optical depth and
10 the Slope factor are assumptions for the observation with the lowest optical thickness (green in Figure 8).

Color	Solar Longitude	Mars Year	Incidence	Emergence	Phase	$\tau(0.9\mu\text{m})$	S ("Slope factor")	RMS (%)
Black	152.3°	27	46°	4°	45°	0.78	1.5	0.05
Purple	187.0°	27	39°	9°	45°	0.87	1.8	0.04
Blue	243.0°	27	72°	2°	73°	1.12	2.6	0.07
sky blue	314.4°	27	16°	10°	19°	1.09	1.2	0.04
Green	92.8°	28	63°	2°	63°	0.25	1.8	-
light green	176.7°	28	66°	56°	93°	0.95	2.1	0.18
Orange	213.7°	28	61°	1°	60°	0.75	2.6	0.12
Red	273.0°	28	10°	1°	11°	3.38	1.6	0.13

11

12

13

14

15

16

17

18

19

1 Figures and Figures Captions

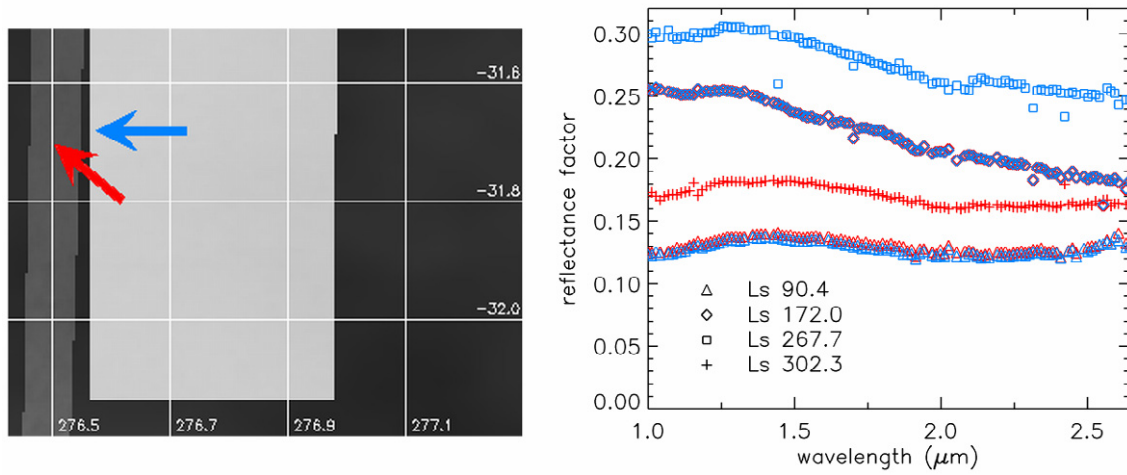


Figure 1 : Left: albedo map constructed with 3 observations obtained at different solar longitudes. 2 narrow tracks (dark and light grey, $L_s 302.3^\circ$ and $L_s 267.7^\circ$ respectively) overlap a wide track (black, $L_s 90.4^\circ$). Another wide track has been obtained at $L_s 172^\circ$. Two nearby regions (red and blue arrows) have been selected within the narrow tracks. Right: spectra of the two selected regions for different values of L_s . They are similar for the two wide tracks which cover both regions (triangles and diamonds), demonstrating that the reflectance properties of the red and blue areas are similar. It is therefore possible to include spectra of these two areas obtained at different values of L_s (blue squares and red crosses) in a single time series from $L_s 90.4^\circ$ to $L_s 302.3^\circ$.

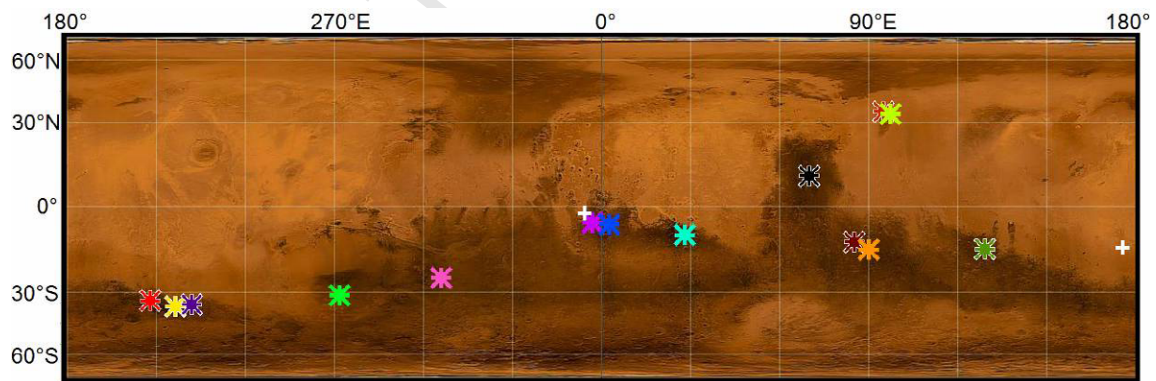


Figure 2 : Locations of the selected time series on a background of a cloud-free mosaic constructed from MGS images obtained during the period 1999 to 2001 (Geissler, 2005, modified by Szwasz et al., 2006). The two white crosses indicate the position of the MERs Opportunity (near 0°) and Spirit (near 180°).

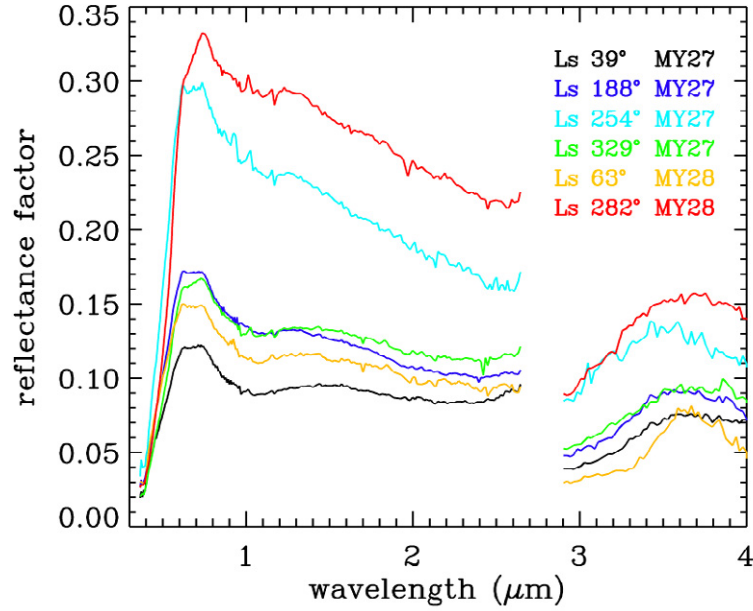


Figure 3 : Time series of observed reflectance spectra for the region at 70.1°E, 13.2°N (Syrtis Major). Solar longitudes and Martian years (using the numbering of Clancy et al., 2000) are indicated. Wavelengths > 2.9 μm are processed using the approach of Jouglet et al. (2008). A wide diversity of spectra is observed. Black: low atmospheric contribution. Yellow: the absorption bands at 1.5 μm , 2 μm and the shape of the 3 μm band are indicative of water ice clouds (Langevin et al., 2007). Light blue: a strong decreasing slope is observed at high solar zenith angle (80°). Red: July 2007 dust storms. Dark blue and green: significant differences in spectral slope (15% and 30%) are observed even for spectra with similar albedo levels.

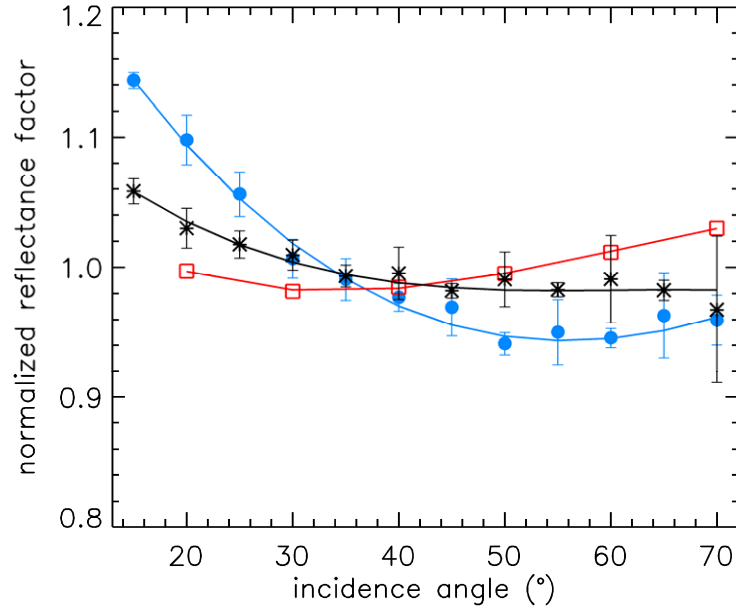


Figure 4 : Laboratory measurements of the reflectance factor in the near-IR ($\lambda \sim 1 \mu\text{m}$) for a nadir viewing geometry and different incidence angles (Pommerol and Schmitt, 2008). Red squares ($\lambda = 1 \mu\text{m}$): small-grained volcanic tuff (radius: 25-50 μm). Black crosses ($\lambda = 1.3 \mu\text{m}$): small-grained volcanic tuff (radius: 25-50 μm) covered by mm size grains of the same material (surface coverage by large grains: 30-35%; grains are partially buried). Filled blue circles ($\lambda = 1 \mu\text{m}$): mixture of sand-sized grains (radius ranging from 140 μm to >600 μm) of a dark basalt (in agreement with thermal inertia measurements of dark regions, see e.g. Palluconi and Kieffer, 1981). Each point is the average of 20 measurements, with standard deviations indicated as “error bars”. Lines correspond to a third order polynomial fit of each analogue.

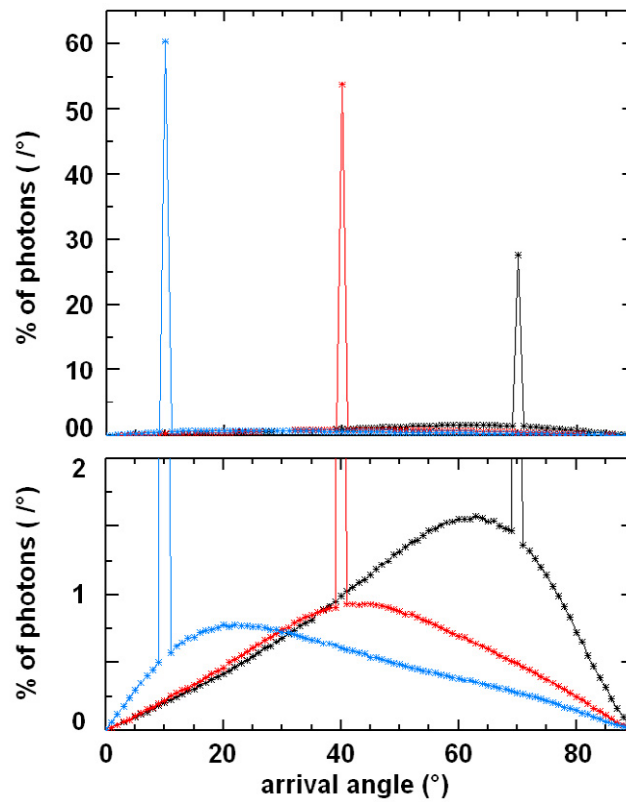


Figure 5: Distribution of photons that reach the surface as a function of the arrival angles (0° is zenith). Simulations are performed using the model and aerosols parameters described by Vincendon et al. (2007). The aerosols optical depth is 0.6. Three different solar incidence angles are shown ($i=10^\circ$, blue; $i=40^\circ$, red; and $i=70^\circ$, black).

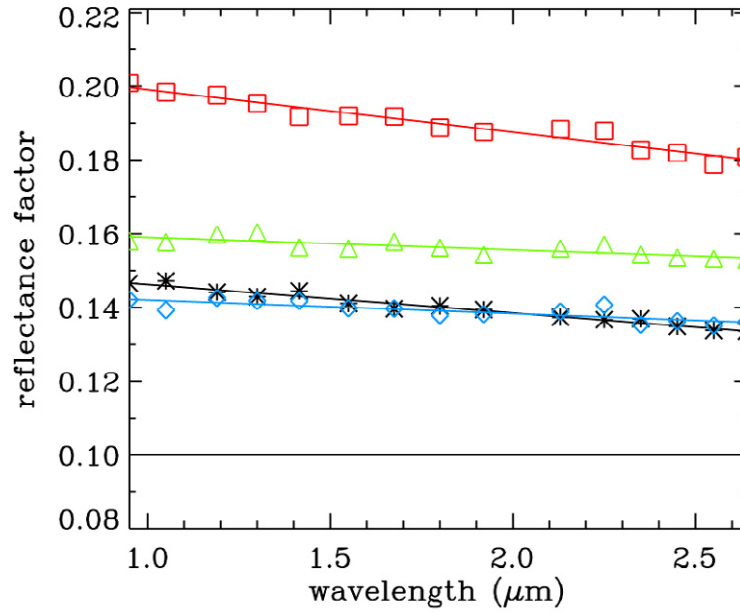


Figure 6 : Modeled near-IR reflectance spectra as seen above a dark surface (albedo of 0.10, solid black line) through an aerosols layer (constant optical depth of 0.8) with the wavelength dependent phase function computed with the monomodal size distribution described in the text. The viewing geometry is nadir with different solar incidence angles, i , shown. Red squares: $i=80^\circ$; green triangles: $i=60^\circ$; blue diamonds: $i=40^\circ$; black stars: $i=10^\circ$. Modeled RF are calculated for 15 wavelengths (symbols); Smooth interpolated lines are indicated. A wavelength dependent phase function can create a varying decreasing slope in the light backscattered by aerosols. However, the amplitudes of resulting variations are small compared to observations.

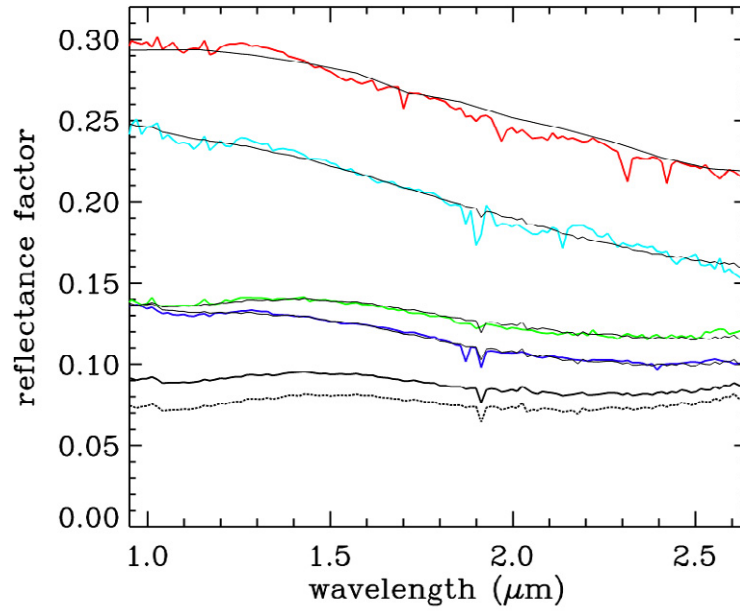


Figure 7: Time series of observed spectra (thick solid color lines) for a region at 70°E , 13°N (Syrtis Major). The reflectance spectrum of the surface derived from observations with a low optical thickness is indicated as a dotted line. Best fit models for the observations are shown as thin solid lines. The solar longitude, the photometric angles and the results of the model fit are indicated in Table 1.

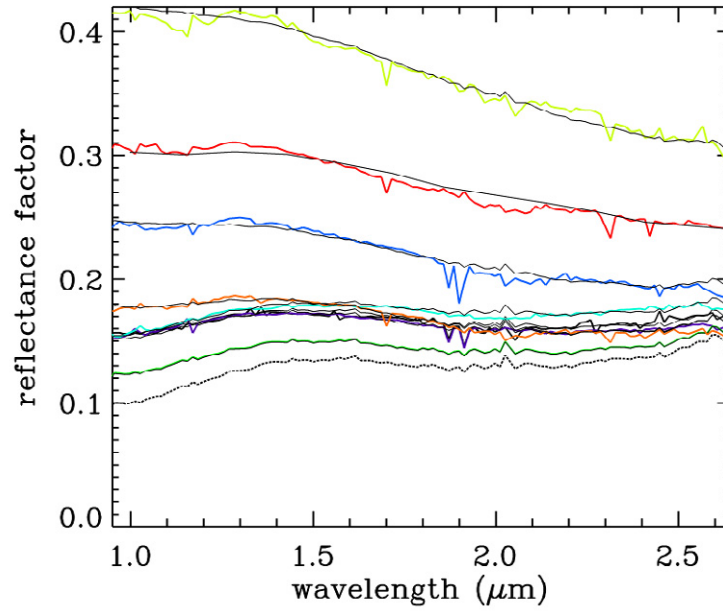


Figure 8: Time series of observed spectra (thick solid color lines) for a region at 208°E, 34°S (Sirenium). The reflectance spectrum of the surface derived from observations with a low optical thickness is indicated as a dotted line. Best fit models for the observations are shown as thin solid lines. The solar longitude, photometric angles and results of the model fit are indicated in Table 2.

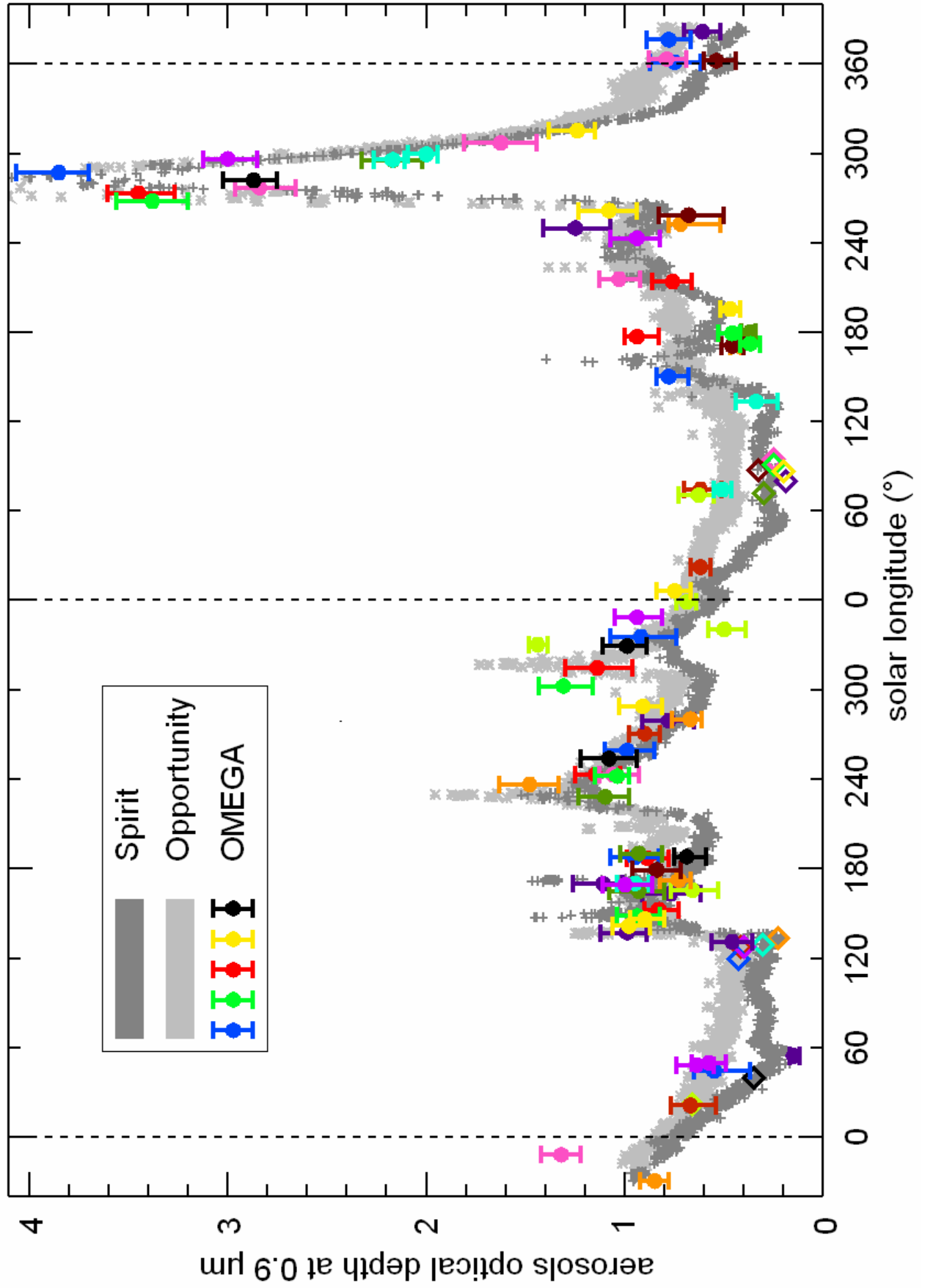


Figure 9 : Derived optical depths at $0.9\mu\text{m}$ using OMEGA observations over dark surfaces (color points; relative error bars are indicated), plotted with PanCam/MERs nearly-simultaneous measurements of the optical depth at $0.9\mu\text{m}$ (Lemmon et al., 2004, 2006 and personal communication; stars: Opportunity; crosses: Spirit). OMEGA retrievals use the phase function of Ockert-Bell et al. (1997). Each color corresponds to a different surface region (see Figure 2 for the location). Diamonds indicate the assumed optical depth of the correction for the low optical depth spectrum of each sequence.

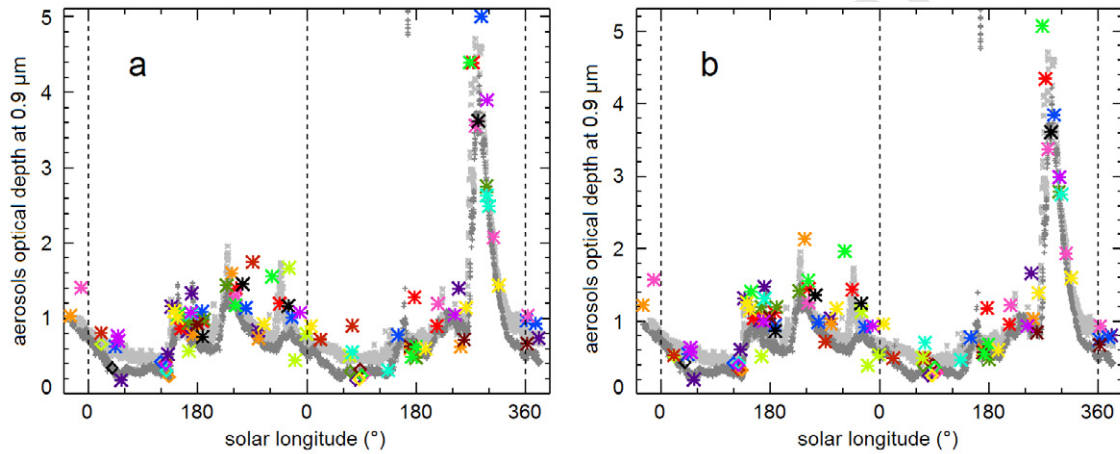


Figure 10 : Same as Fig. 9 but for different assumptions: a. We use the phase function of Tomasko et al. (1999). Optical depths are changed by a factor between 0.9 and 1.4 compared to the Ockert-Bell et al. function. b. Retrieved optical depth with the Ockert-Bell phase function are scaled at an altitude of -1.7 km corresponding to the MER landing sites. We assume an exponential atmosphere and a constant scale height of 11.5 km to approximate well-mixed conditions. The elevation of the regions analyzed here varies between -4.5 and 3 km , which correspond to scaling factors that range from 0.7 to 1.3.

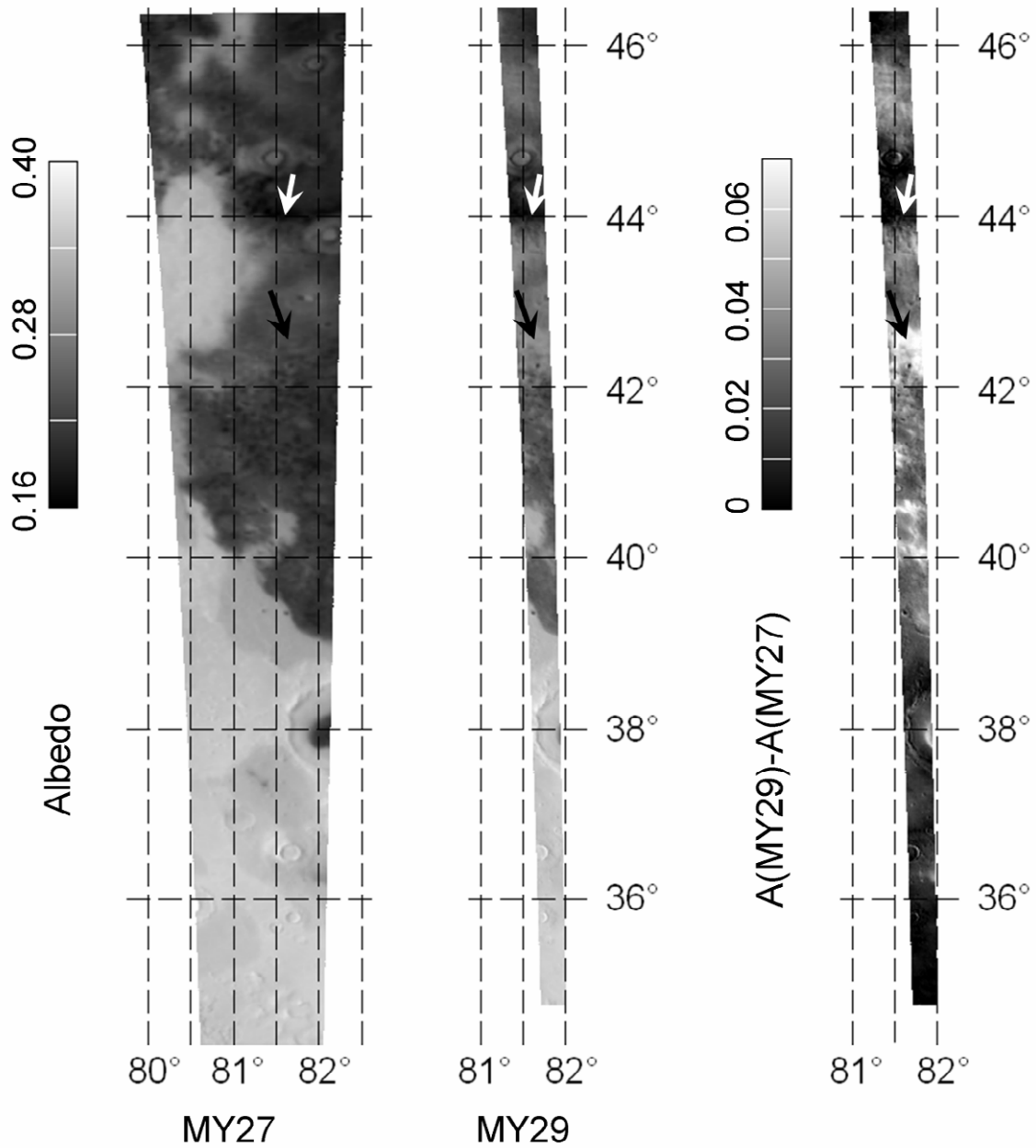


Figure 11 : Left and middle: « Albedo maps » (RF at $1.08\mu\text{m}$) of the Nilosyrtris region that have undergone recent surface albedo changes (Geissler et al., 2005). Left: Ls 98° of MY27 (October 2004); Middle: Ls 20° of MY29 (January 2008), 30° of Ls after the decay of a global dust storm. The two regions are observed with similar solar zenith angles (between 55° and 60°) and low optical depths according to MER measurements (approximately 0.4 for Ls 98° and 0.6 for Ls 20°). Right: albedo differences between MY29 and MY27. The albedo features are basically similar after and before the dust storm. Some places (notably that indicated by the black arrow) appear brighter, while others (white arrow) show nearly no changes of spectral properties (see Fig. 12).

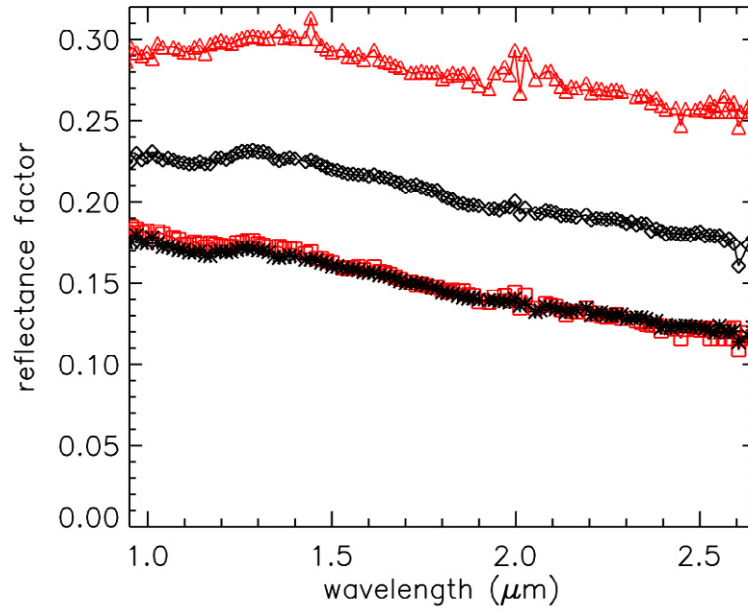


Figure 12 : Spectra corresponding to the regions highlighted by the arrows in Fig 11. Black symbols correspond to Ls 98°, MY 27 and red symbols to Ls 20°, MY 29. Most regions are the same before and after the dust storms (stars and squares: white arrow in Fig. 11), but some regions undergo brightening (triangle and diamonds: black arrow in Fig. 11). Spectra in that region show a strong decreasing slope even under low aerosols contribution, which could indicate a partial surface dust coating (Fischer and Pitters, 1993).

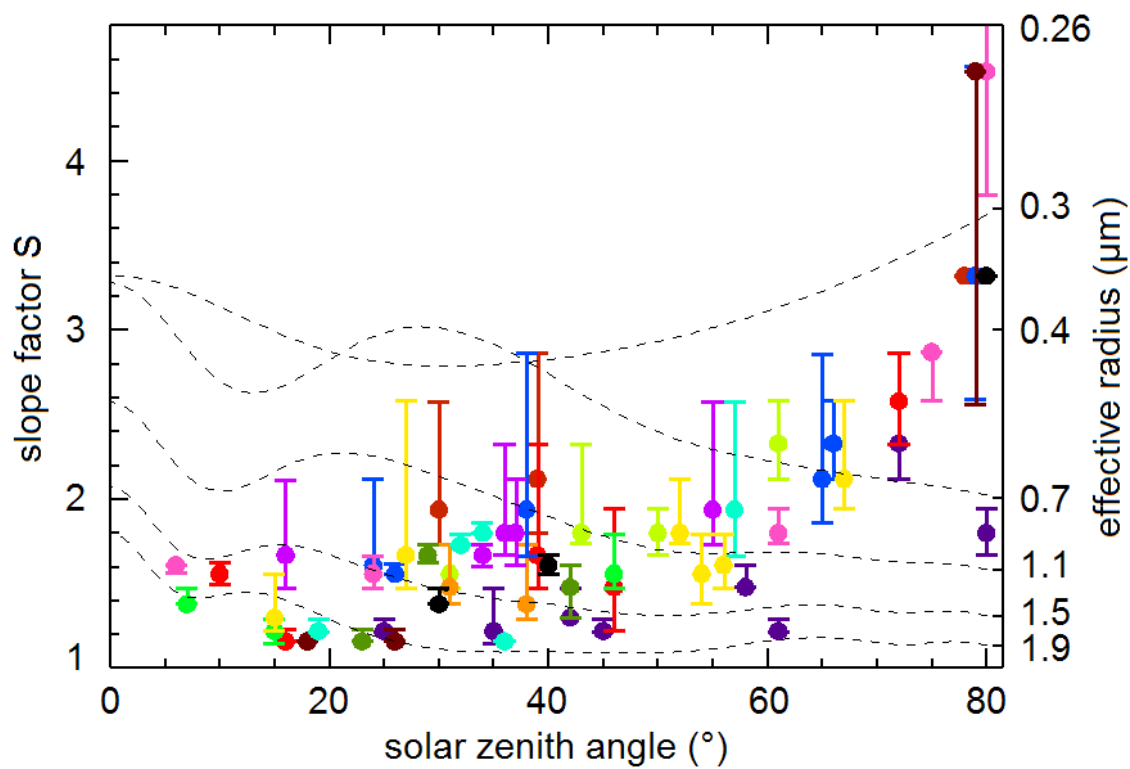


Figure 13 : Variations of the slope factor S as a function of the solar incidence angle (color points; relative error bars are indicated). The corresponding effective particle sizes are indicated with dotted lines (right y-axis). Particles vary with time within the $1\mu\text{m} - 2\mu\text{m}$ range for low to moderate incidence angle. Smaller mean particle sizes ($< 1\mu\text{m}$) are seen at high solar incidence angle ($> 60^\circ$). Observations with emergence angles greater than 40° are not considered, as well as points for which the error bar is greater than two.

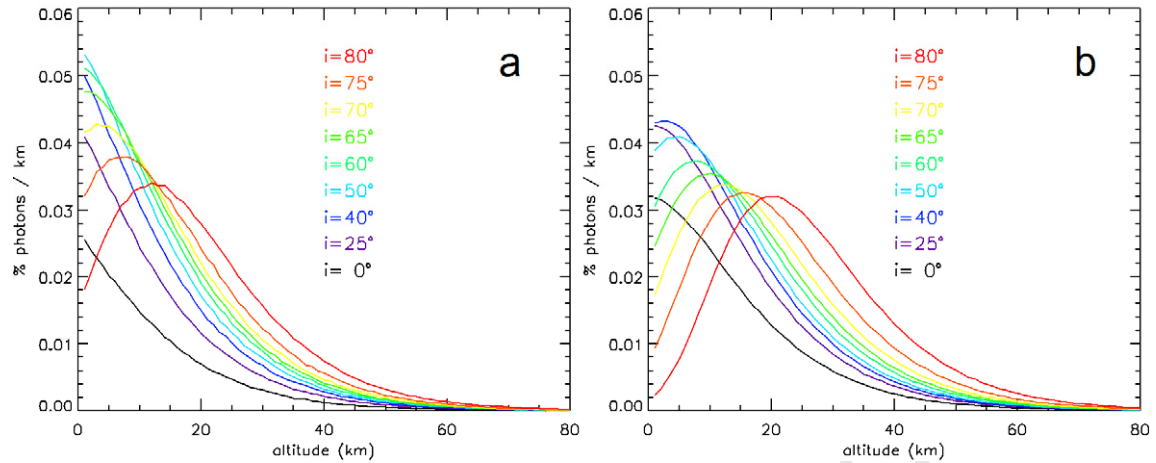


Figure 14 : Distribution of photons as a function of the altitude for the first interaction event (with dust aerosols) for different solar incidence angles. The dust optical depth varies with altitude with a scale height of 11.5km. The total optical depth is 0.5 (a) and 1 (b). The altitude at which photons interact with aerosols increases with incidence angle, i.e., photons interact higher in the atmosphere at higher optical depth.

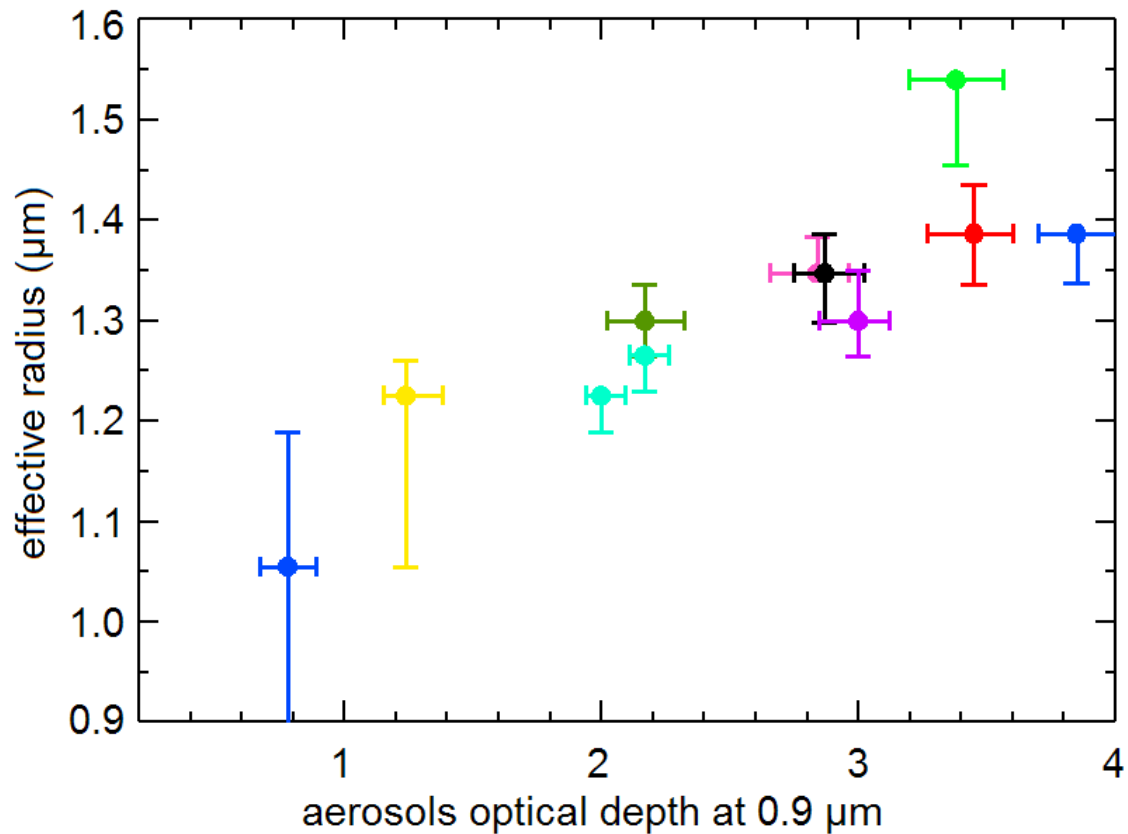


Figure 15 : Variations of the effective radius of aerosols as a function of the optical depth during and after the July 2007 dust storm ($L_S > 265^\circ$, MY28). We have selected observations with solar zenith angle $< 70^\circ$. Relative error bars are indicated (see section 4.1 for details) The particle size decreases during the decay of the dust storm, which indicates that large particles settle faster than small particles.